UNIVERSITY OF CALIFORNIA

SANTA CRUZ

EVALUATING SHALLOW SLIP EXTENT IN LARGE MEGATHRUST EARTHQUAKES BY ANALYZING P AND PDIFF CODA ARRIVALS FOR WATER REVERBERATIONS

A thesis submitted in partial satisfaction
of the requirements for the degree of

MASTER OF SCIENCE

in

EARTH SCIENCES

by

Andrea Rhode

March 2019

The Thesis of Andrea Rhode
is approved:

_____
Professor Thorne Lay, Chair

_____
Professor Susan Schwartz

_____
Professor Emily Brodsky

_____
Lori Kletzer
Vice Provost and Dean of Graduate Studies

Table of Contents

List of Figures

List of Tables

Abstract
Evaluating Shallow Slip Extent in Large Megathrust Earthquakes by Analyzing P and Pdiff Coda Arrivals for Water Reverberations
Andrea Rhode

Observations of shallow focus megathrust earthquakes are difficult to obtain due to limited instrumentation in the near-source underwater region, and teleseismic observations have limited resolution that is strongly influenced by poorly resolved shallow seismic velocity structures near the toe of the accretionary prism (Lay et al., 2012). Slip under deep water can establish strong water reverberations that persist into seismic coda that is not usually inverted for the source. In this study, P wave coda is examined for many recent major and great earthquakes with independently determined slip distributions and known tsunami excitation to evaluate the prospect for rapidly constraining the up-dip rupture extent of large megathrust earthquakes. For narrowband filtered (7-15 s) data at an 80°-120° distance range, final event average rms Pcoda/rms P (RMS C/P) ratios above 0.610 are found exclusively for events that are believed to have ruptured to shallow depths, while ratios < 0.610 are found for all but one of ruptures that did not extend to the trench. Average RMS C/P ratios computed at all azimuths for each event are larger at azimuths in the direction of the trench for all cases, and events with deep slip beneath continental margins have pronounced reduction of reverberative coda amplitudes in the landward directions. This procedure is successful in separating ruptures that have shallow slip from those that do not for events larger than M_W 7.5. It is likely to be very effective for smaller events as well, as their entire rupture area will span a smaller depth range than for many of these events. Given the overall success of the classification using all

azimuths, which is the simplest for fast implementation, an optimal azimuthal windowing measure is not necessary. Our specific procedure is of somewhat limited value for assessing likelihood of enhanced tsunami excitation relative to the seismic moment magnitude of the event for very nearby coastlines; however, it could still be valuable for tsunamis with coastal arrival times that are longer than the average 15-18-minute lag time required for measuring numerous relative coda levels in the 80°-120° distance range.

1. Introduction

Large oceanic thrust faulting earthquakes occur along plate boundary megathrust faults, which vary in their frictional properties both along strike and with depth (e.g., Lay et al., 2012) and exhibit complex earthquake patterns (e.g., Kanamori, 2014). Many large interplate thrust earthquakes have ruptures confined to the central and deeper portions of megathrusts from 15 to 50 km deep, with relative tsunami excitation mainly being controlled by their seismic moments. Some very large megathrust ruptures initiate in the central depth range of the megathrust and extend upward into the shallow interface in the near-trench, deep-water region, augmenting their excitation of tsunamis (Lay, 2015). Other large ruptures nucleate and rupture at shallow depths less than 15 km on the megathrust, with unusually long rupture durations and strong tsunami excitation, leading to their designation as "tsunami earthquakes" (Kanamori, 1972). Determining the up-dip rupture extent of large megathrust ruptures is important for understanding their overall tsunami excitation, for early evaluation of their potential for being a tsunami earthquake with attendant enhanced tsunami amplitudes, for evaluation of whether lack of shallow coseismic slip indicates potential for a subsequent tsunami earthquake, and for examining depth-varying frictional properties of the shallow megathrust.

Resolving the up-dip limit of rupture for megathrust earthquakes is difficult, mainly due to limited instrumentation in the offshore environment near the toe of the accretionary prism. On-land geodetic observations provide very little resolution of the

up-dip limit of offshore thrust faulting (e.g., Sun et al., 2017; Lay, 2018), and only a few regions have seafloor instrumentation extending out to the trench. Repeat imaging of the seafloor bathymetry can reveal slip to the trench, but this requires high precision measurements before and after large events, which has only been performed in a few cases (e.g., Fujiwara et al., 2011; Maksymowicz et al., 2017). Teleseismic observations have limited resolution of very shallow slip in finite-fault inversions due to limited knowledge of the shallow seismic velocity structure and due to the strong interference produced by depth phases (Lay et al., 2012).

In the absence of real-time direct seafloor geodetic observations, there is a need for a generally applicable strategy for quickly (or retrospectively) inferring the likelihood that a given megathrust event involved significant slip at shallow depth. When slip occurs beneath deep water, up-going seismic wave energy can generate strong acoustic water reverberations (pwP) that generate persistent teleseismic P wave coda well beyond the total rupture duration. Standard procedures used in finite-fault inversions tend to exclude the coda as it is not usually well accounted for by uniform layered structures commonly used to invert for the slip distribution. Theoretically, one could invert for slip models using complete calculations of teleseismic signals for 3D structure in the shallow megathrust environment, accounting for water reverberations above variable bathymetry and in the presence of strong seismic velocity heterogeneity in the subsurface, but this has only recently become viable

(Qian et al., 2019), and it remains very difficult to implement for rapid determination of finite-fault inversions that require computation of many Green's functions.

Azimuthal variations are expected in the water multiples for submarine megathrust events, whether slip is shallow or deep. However, the first order effect of variable strength of pwP excitation as a function of depth of slip on the fault should be observationally detectable without comprehensive modeling. In this study, the relative rms amplitude of teleseismic P wave coda to rms amplitude of direct P wave arrivals for data at epicentral distances from 80° to 120° is examined for 39 $M_W \geq 7.5$ earthquakes from 1990 to 2018. Using independently determined slip distributions from finite-fault inversions and known levels of tsunami excitation, straightforward measures of the seismic data at large distances are used to evaluate the prospect for rapidly constraining the up-dip rupture extent of large megathrust earthquakes. Potentially, such a strategy, applied within up to 18 minutes after an event could indicate whether shallow slip in the earthquake has enhanced the tsunami warning urgency relative to that inferred from rapidly estimated M_W and point-source moment tensor alone. The procedure can also be applied to evaluate up-dip rupture extent for historic events for which we have limited seismic observations (e.g., Kanamori et al., 2019), and that could greatly impact assessment of potential for tsunami earthquake occurrence up-dip of previous great megathrust failures. There is potential for faster analysis of coda excitation for closer distances, using the strategy demonstrated here,

but procedures will need to be adapted to cope with the arrival of seismic phases after P.

Seismic coda is traditionally defined as scattered waves generated when direct waves interact with small-scale (less than a wavelength) random heterogeneities in the medium (Aki and Chouet, 1975), but coda also explicitly includes reverberations within layered structures. These scattered waves repeatedly sample the region near the source and receiver, producing a continuous wavetrain comprised of the interfering scattered arrivals following the direct P and S wave arrivals. Ward (1979) was the first to identify pronounced 'ringing' in the coda portion of azimuthally distributed P wave phases from large oceanic earthquakes, and suggested that such ringing P waves could be attributed to shallow focus events with high tsunamigenic potential. He asserted that the oceanic column is an effective waveguide for favorably excited compressional modes that leak into the water later (Figure 1.1a). This assertion was supported in studies by Wiens (1987, 1989) that demonstrated that the presence of a deep-water column overlying the seismic source enhanced P wave coda reverberation amplitudes. Additionally, he showed that a slightly dipping water-solid interface resulted in much stronger oscillations in the P wave coda than for a flat surface 1D model (Figure 1.1b), with complex azimuthal variations.

At teleseismic distances, P wave coda oscillations are readily observed in the interval between the direct P and PP waves on vertical component seismograms. For example,

Ihmlé and Madariaga (1996) identified water reverberation phases within the P to PP wave interval from two great subduction zone events; 1995 Chile (M_W 8.1) and 1994 Kurile Islands (M_W 8.3). They did not fully quantify the signals, but found that the energy originated near the oceanic trenches.

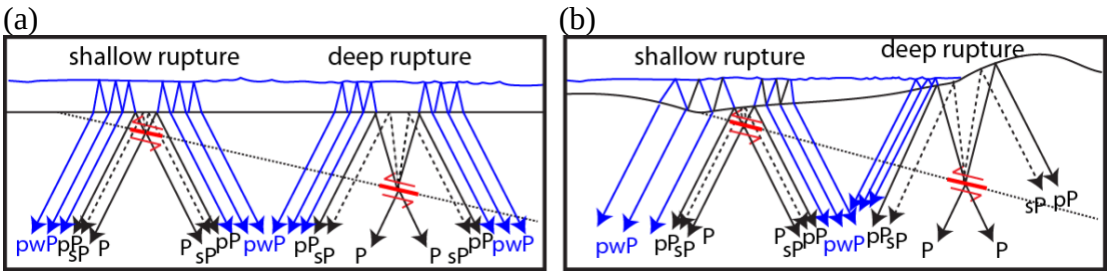

Figure 1.1 Schematic representation of **(a)** a 1D water layer with acoustic wave reverberations (pwP) that generate teleseismic P wave coda in all directions and **(b)** a 2D water layer with pwP that generate azimuthally varying teleseismic P wave coda.

Some simple 1D velocity structure synthetic calculations using a propagator matrix method are useful for understanding the water multiple behavior. Figure 1.2 shows teleseismic ground motion calculations for point-source thrust faulting for structures with either 3 km or 6 km deep water layers over an elastic half-space, with either a 20 s duration triangular source time function or a 60 s duration triangular source time function. Far-field ground motions are computed at two azimuths, one with direct P wave take-off angle near the downgoing P wave radiation node, and the other with take-off angle near the P wave radiation max. If the water is 3 km deep, low amplitude, rapidly decaying short-period (~ 5 s) oscillations are produced at both azimuths for 20 s and 60 s duration sources, whereas larger, longer period (~ 10 s) oscillations are produced by the pwP in the 6 km deep water layer. The differences are readily observed for the shorter duration source, but for the 60 s duration source

the large long-period energy in the direct P (+pP+sP) waveform causes the ringing coda to be relatively low amplitude. By filtering the data in the 0.05-0.2 Hz (20-5 s) passband, the ringing coda is seen to be comparable to the energy in the P wave during the 60 s source duration for the deep-water case. These 1D model calculations are representative of Figure 1.1a, with the uniform layer giving only secondary azimuthal variation in the coda amplitudes. There is some variation relative to the P amplitudes due to the radiation pattern effects for the P wave, but this is suppressed by the interference of pP and sP, which also have changing radiation patterns with azimuth.

While the previous studies and Figure 1.2 provide general insight into the nature of pwP reverberations in teleseismic recordings of subduction zone earthquakes, seismograms from large earthquakes are complex and late P wave signals in teleseismic seismograms have not been thoroughly exploited or have even been misinterpreted. For example, a proposed second stage tsunami earthquake at shallow depth during the source rupture process for the 2015 Illapel (M_W 8.4) earthquake was inferred based on observation of prolonged teleseismic P wave ground motions (Lee et al., 2016). However, the 3D method used in that study to compute synthetic ground motions for faulting did not account for pwP water multiples, and Lay et al. (2016), An et al. (2017), and Qian et al. (2019) demonstrate that the arrivals could be explained by improved modeling of the water reverberations without any prolonged

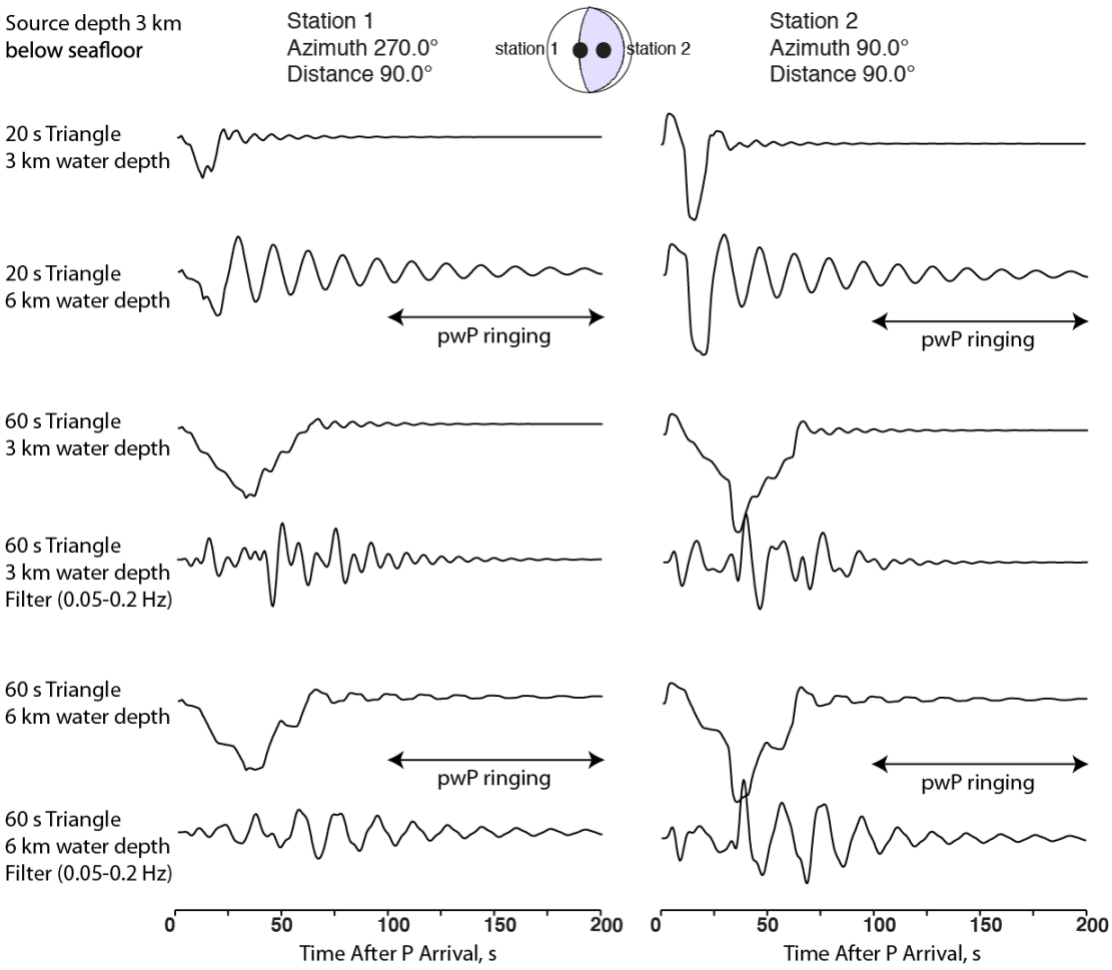

Figure 1.2 Far-field P wave ground displacement calculations at two stations for point source thrust faulting in models with a water layer over an elastic halfspace. The source has either a 20 s duration triangle or a 60 s duration triangle source time function. The water depth is either 3 or 6 km. The text discusses the different cases.

rupture. Nonetheless, ambiguity exists regarding which source rupture attributes and source region structural features are important for exciting strong P coda amplitudes (Ward, 1979; Ihmle and Madariaga, 1996; Yue et al., 2017; Fan and Shearer, 2018, Wu et al., 2018). Recent three-dimensional studies by Qian et al., (2019) and Wu et al., (2018) conclude that the bathymetry and sedimentary layers have strong effects on enhancing P wave coda oscillations in addition to the location of earthquake slip.

Figure 1.1b provides an intuitive framework for anticipating that the up-dip extent of slip on the megathrust during a large earthquake will affect the strength and azimuthal pattern of P coda generation. Shallower slip will occur under deeper water and longer period pwP coda can be generated over a wide range of azimuths; down-dip slip occurs under shallower water that will generate shorter period pwP reverberations with a constrained azimuthal range due to lack of water reverberations caused by shoaling of the ocean. This offers the potential of using the strength of P coda relative to direct P as a proxy for up-dip extent of megathrust slip. This, in turn, will influence tsunami excitation, which will be stronger for shallow slip beneath deep water. Given that the strength of coda waves can be quickly evaluated after arrival of the P signal as long as other major phases are avoided, recognition of the likelihood of slip having extended to the trench with associated enhanced tsunamigenic potential could be achieved within a few minutes after the P arrival, potentially contributing to early tsunami hazard assessment. We explore this concept, using a simple measure of relative rms P wave coda amplitude to rms P wave amplitude (RMS C/P) from vertical component broadband velocity seismograms. We consider 39 recent major earthquakes ($M_W \geq 7.5$) with previously estimated slip distributions to evaluate this approach.

2. Methods

2.1 Data and P and Pcoda Time Windows

All large earthquakes produce teleseismic arrivals that involve a mix of major phases resulting from Earth layering and free surface reflections, along with coda generated by departures from 1D structure as well as layered structures near the source and receivers. Figure 2.1 shows a profile of ground displacement and ground velocity motions for the December 25, 2016 Chile earthquake (M_W 7.6), in the passband 0.005 to 0.2 Hz (200-5 s). The waves are aligned on P, and clear move-out of secondary travel time branches are apparent. In Figure 2.2. the same traces are shown filtered in the passband 0.0667 to 0.1428 Hz (15-7 s). While there is distributed shorter period energy throughout the time window of the profile, the major phases still are evident as they include significant short-period energy. The diffuse energy is the seismic coda, and it accompanies each direct phase. Some of this is generated near the stations or on deep paths, but that component will be incoherent from trace to trace because the station and path structures vary. That part of the diffuse energy that is generated from pwP reverberations near the source will be present for all major P phases, but will not follow SH phases.

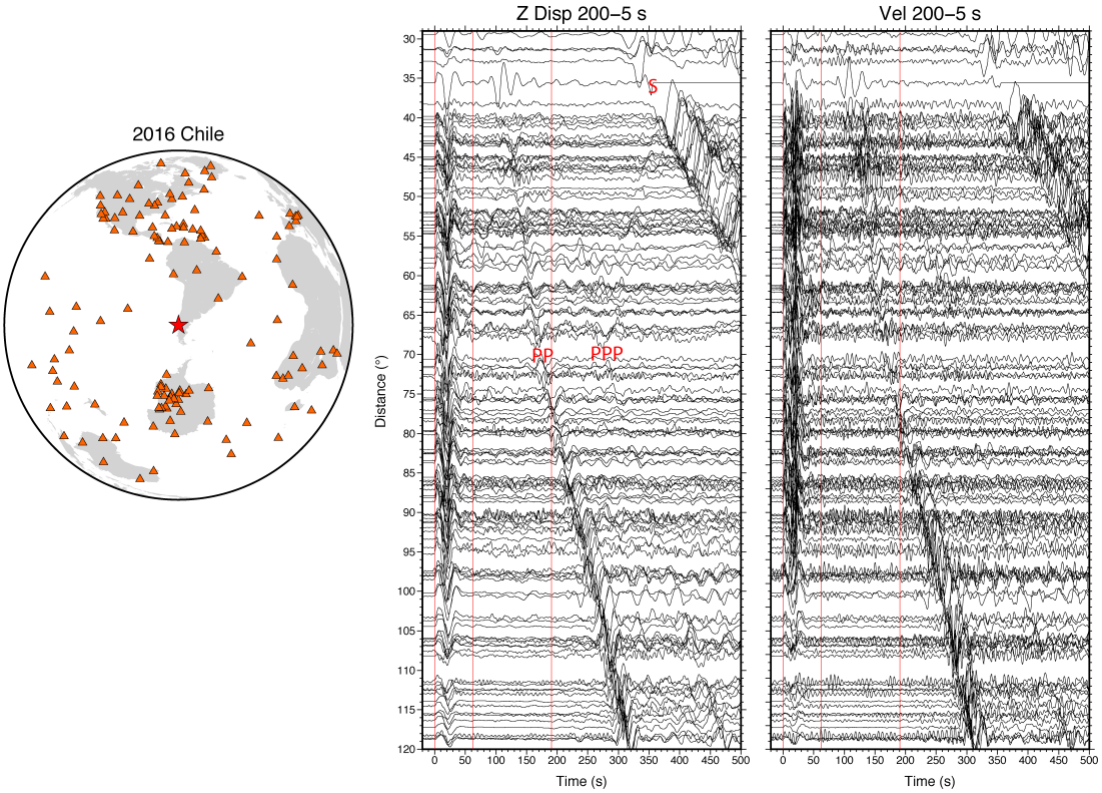

Figure 2.1. Profiles of seismic recordings for the December 25, 2016 (Mw 7.6) Chile earthquake with ground displacements (Disp) and ground velocities (Vel) shown in the distance range 30° to 120°. The data have had instrument responses removed and are filtered in the broad passband of 0.005 to 0.2 Hz (200-5 s). The map on the left shows the station distribution. The data are aligned on the initial P wave arrival. Note the clear move-out of secondary phases following P, including PP, PPP, and S waves. The time interval between first two red lines is the duration of the P wave radiation from the source and between the next two lines is the duration of an interval in the waveforms between P and PP from 80° to 120° that is used for the coda. The amplitude of each trace is normalized by the largest amplitude in the signal.

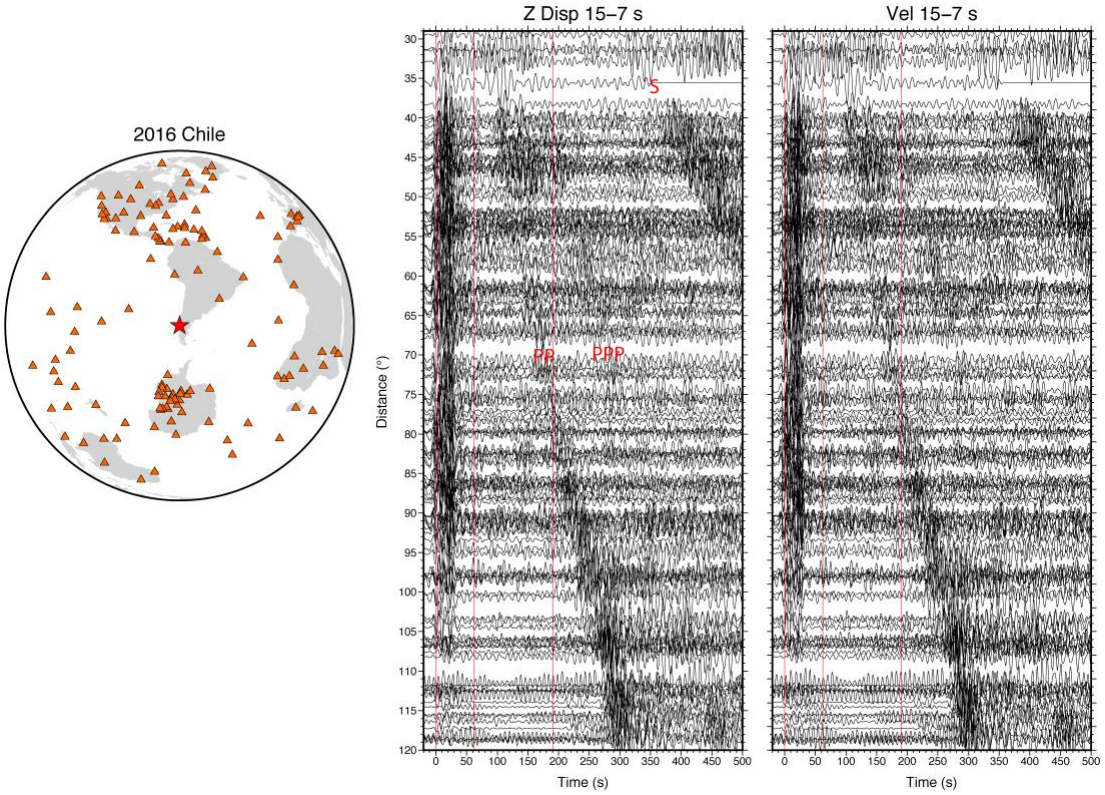

Figure 2.2. Profiles similar to Fig. 2.1, but with the ground displacements and ground velocities filtered in the 0.0667 to 0.1429 Hz (15-7 s) passband. Note that the major secondary arrival branches (PP, S are still very apparent. Also note that the background signals have continuous coda at all distances lower in amplitude than the main phases.

The 2016 Chile earthquake is well-established to have rupture deep on the megathrust, with no indication of shallow near-trench slip (e.g., Melgar et al., 2017). In contrast, the July 30, 1995 Chle (M_W 8.0) earthquake is known to have produced strong teleseismic coda (Ihmlé and Madariaga, 1996) and has been found to have significant slip at shallow depth (Lay et al., in preparation, 2019). Teleseismic data profiles are shown in Fig. 2.3 and 2.4.

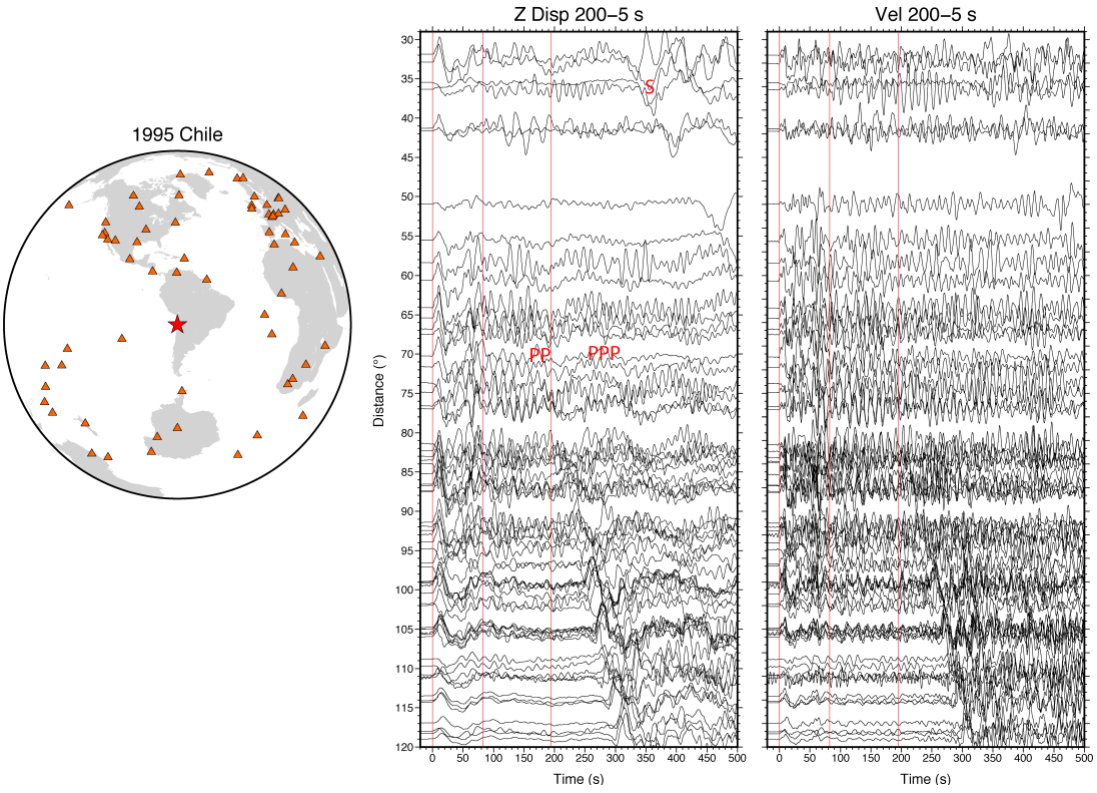

Figure 2.3. Profiles of seismic recordings for the July 30, 1995 (Mw 8.0) Chile earthquake with ground displacements (Disp) and ground velocities (Vel) shown in the distance range 30° to 120°. The data are filtered in the passband 0.005 to 0.2 Hz (200-5 s). The data are aligned on the initial P wave arrival. Note that the strong coda reverberations after the P waves and following PP obscure the secondary arrival travel time branches, particularly in the velocity profile. The first two red lines indicate the duration of the P wave radiation from the source and the last two indicate the duration of the interval in the waveforms between P and PP from 80° to 120° that is used for the coda.

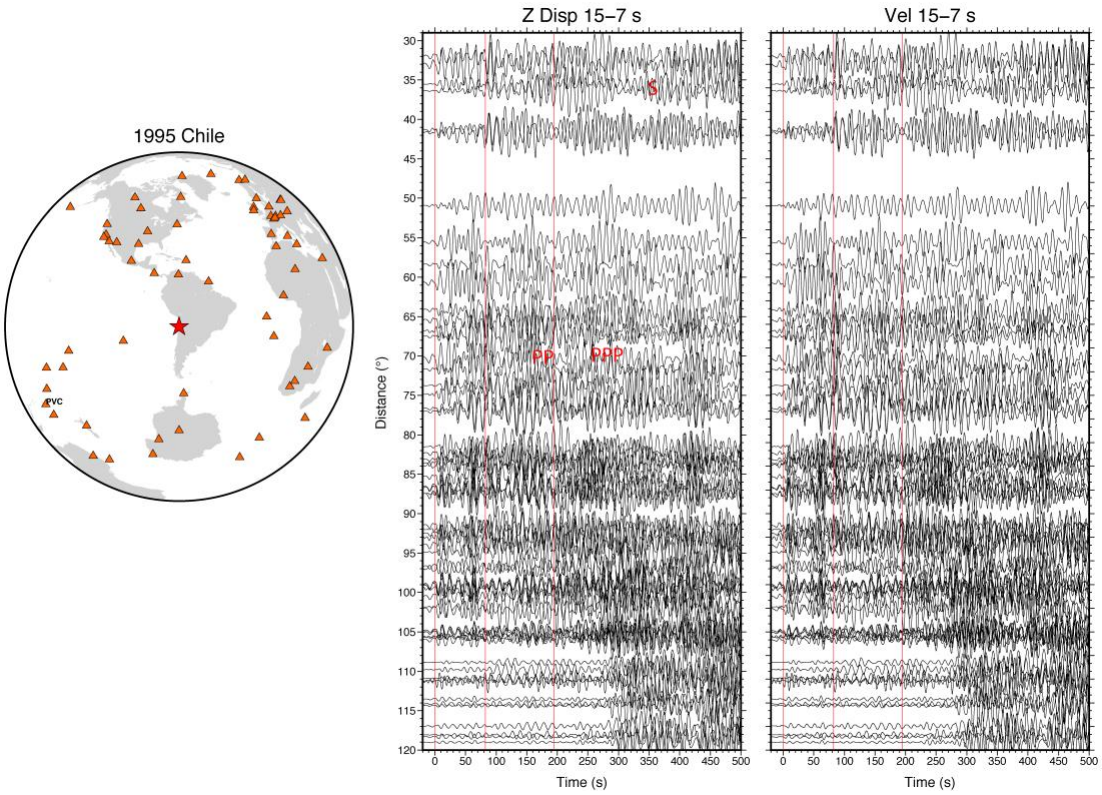

Figure 2.4. Profiles similar to Fig. 2.3, but with the ground displacements and ground velocities filtered in the 0.0667 to 0.1429 Hz (15-7 s) passband. Note that the nearly continuous coda obscures the secondary arrivals, relative to the same passband for the 2016 Chile event in Fig. 2.2. Diffraction beyond 100° weakens the overall signal relative to later arriving PP, which is not diffracted.

Referring to the IASP91 travel time curves for a surface source, shown in Fig. 2.5, it is clear that the most favorable distance range for observing a significant time interval of P coda free of large secondary arrivals is from about 80° to 120°.

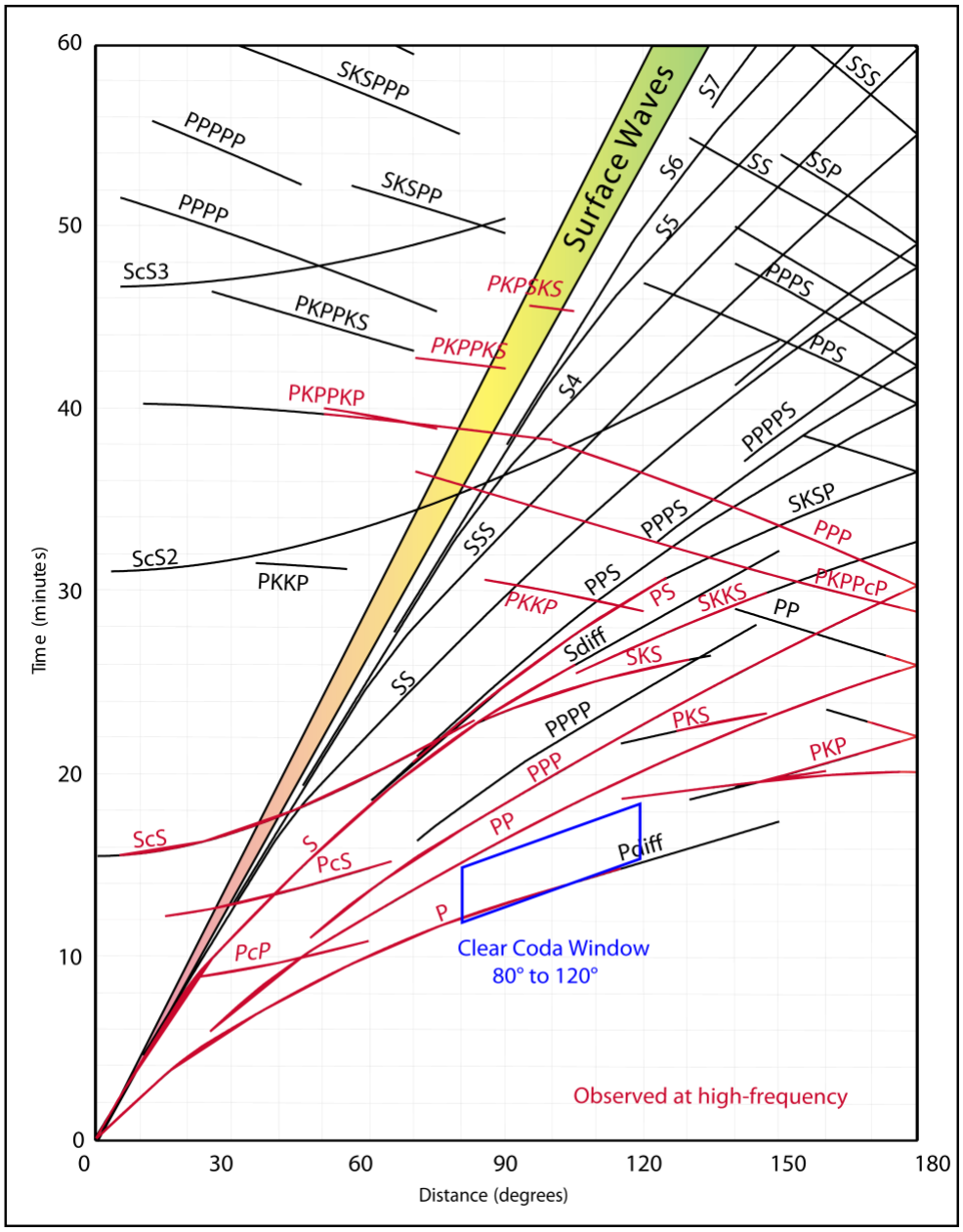

Figure 2.5. Travel time curves for a surface source for the IASP91 model. The distance window from 80° to 120° has a several minute-long time window for observing the direct P and early P coda energy (blue quadrilateral). Red curves indicate branches that are commonly observed to have short-period energy in teleseismic data.

To evaluate the potential use of P coda for constraining up-dip rupture extent, vertical component broadband recordings for 39 very large magnitude (M_W > 7.5) subduction zone earthquakes (Figure 2.6, Tables 1.1, 1.2) recorded at all azimuths for epicentral distances between 80° and 120° were downloaded from IRIS (www.iris.edu). The distance window was chosen to ensure that the time separation between the initial P

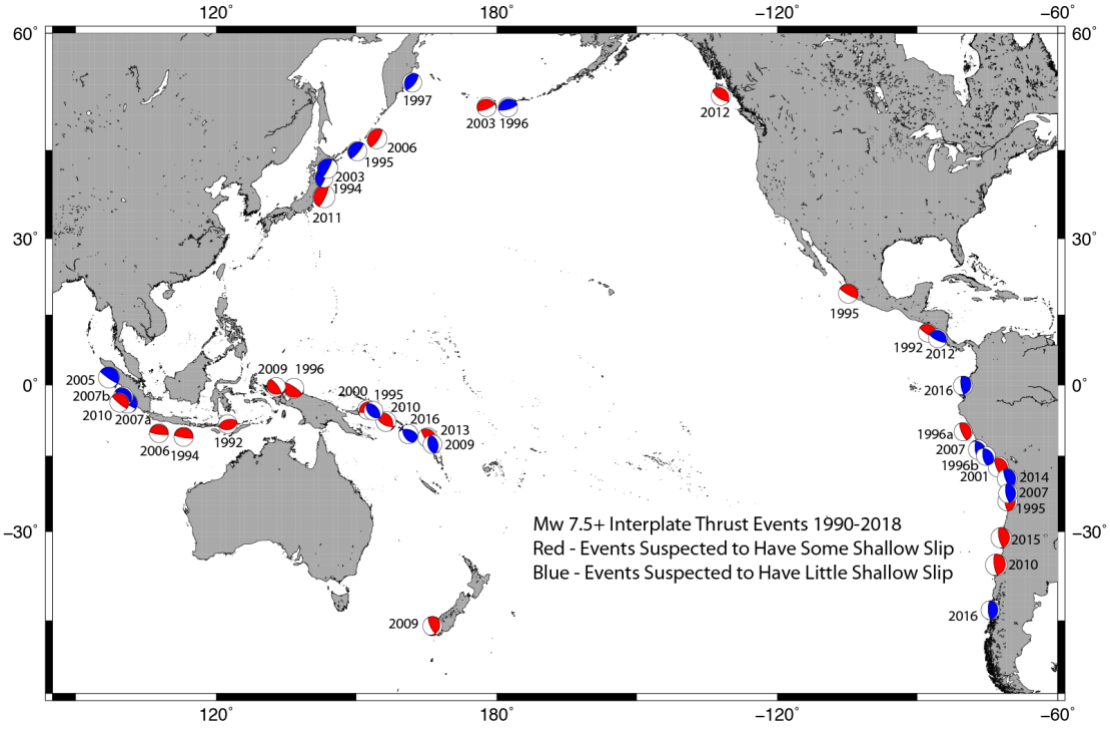

Figure 2.6. Event map of major and great interplate thrust events from 1990 to 2018. The teleseismic P (and Pdiff) signals from 80-100° to 115-120° from all 39 events are analyzed here. Based on examination of published finite-fault models for these events, we characterize each as either suspected to have some shallow slip (or entirely shallow slip, for tsunami earthquakes) (Table 1.1), or suspected to not have significant shallow slip (Table 1.2).

Table 1.1 Events with some shallow rupture

Location	Date	Time	Latitude	Longitude	Hc (km)	Mw	Min GCARC	Max GCARC	GMCT Td (s)	Ye et al. Td (s)	Tcoda end (s)	RMS C/P
Nicaragua	09/02/92	0:16	11.74	-87.34	12.4	7.65	83	117	109	120	200	0.794
Flores	12/12/92	5:29	-8.5	121.9	17.2	7.77	82	118	65	71	197	0.957
Java	06/02/94	18:17	-10.48	112.84	15.4	7.79	80	117	98	84	190	0.617
Chile	07/30/95	5:11	-23.34	-70.27	37.0	8.02	81	120	86.8	82.5	194	1.401
Mexico	10/09/95	15.35	19.05	-104.2	15.5	8.01	80	120	86.2	99.5	190	0.691
Indonesia	02/17/96	5:59	-0.92	136.98	14.9	8.33	81	120	86.2	91	194	0.911
Peru	02/21/96	12:51	-9.59	-79.59	13.6	7.53	80	118	65.4	99	190	0.618
Papua	11/17/00	21:01	-5.49	151.88	16.1	7.80	80	120	67.2	81.5	190	0.952
Peru	06/23/01	20:33	-16.38	-73.5	18.1	8.41	100	115	158.4	129.5	255	0.781
Aleutian	11/17/03	6:43	51.12	178.65	24.6	7.78	80	115	68.4	59	190	1.095
Java	07/17/06	8:19	-9.32	107.33	11.9	7.74	100	120	159.2	164.5	220	0.939
Kuril	11/15/06	11:14	46.58	153.27	15.0	8.33	100	120	120.4	133.5	220	0.610
Solomon	04/01/07	20:39	-8.43	157.06	14.8	8.10	100	115	105	124.5	255	0.909
New Zealand	07/15/09	9:22	-45.76	166.56	17.6	7.81	100	120	61.2	50	220	0.754
Chile	02/27/10	6:34	-36.12	-72.9	28.3	8.81	100	115	137.8	142	255	0.954
Mentawai	10/25/10	14:42	-3.49	100.08	12.3	7.85	90	120	94.6	117.5	220	0.898
Tohoku	03/11/11	5:46	38.3	142.37	16.1	9.12	100	115	159.6	177.5	255	0.816
Santa Cruz Islands	02/06/13	1:12	-10.74	165.14	64.2	7.95	80	120	78.4	90	190	1.172
Central Chile	09/16/15	22:54	-31.573	-71.674	22.4	8.3	100	120	120	113.5	220	0.879
Immature Subduction Zones (?)												
Papua	01/03/09	19:43	-0.41	132.89	14.2	7.70	90	120	56.6	44.5	220	0.392
Haida Gwaii	10/28/12	3:04	52.79	-132.1	57.4	7.80	80	116	76.8	71	190	0.510

Table 1.2 Events without shallow rupture

Location	Date	Time	Latitude	Longitude	Hc (km)	Mw	Min GCARC	Max GCARC	GCMT Td (s)	Ye et al. Td (s)	Tcoda end (s)	RMS C/P
Honshu*	12/28/94	12:19	40.54	143.43	27.6	7.76	80	119	91	55	190	0.584
Solomon	08/16/95	10:27	-5.78	154.29	45.4	7.74	82	120	88.6	66	197	0.536
Kuril	12/03/95	18:02	44.71	149.26	25.5	7.91	80	117	76.8	71	190	0.396
Aleutian	06/10/96	4:03	51.59	-177.6	21.7	7.90	81	116	76	73.5	194	0.555
Peru	11/12/96	16:59	-14.96	-75.56	34.2	7.74	83	116	83.6	65	200	0.686
Kamchatka	12/05/97	11:26	54.8	162	42.8	7.78	82	118	73.2	72	197	0.519
Hokkaido	09/25/03	19:50	41.86	143.87	28.7	8.20	80	120	83.6	77	190	0.348
Sumatra	03/28/05	16:09	2.09	97.11	28.2	8.65	90	119	130	162	220	0.596
Peru	08/15/07	23:40	-13.38	-76.61	29.4	8.00	100	120	140	127	220	0.594
Sumatra	09/12/07	11:10	-4.44	101.37	30.9	8.52	100	115	117.6	129	255	0.605
Sumatra	09/12/07	23:49	-2.66	100.83		7.91	80	120	83.2	91	190	0.403
Chile	11/14/07	15:40	-22.25	-69.89	36.7	7.75	100	120	61.4	64.5	220	0.435
Costa Rica	09/05/12	14:42	10:12	-85.35	22.3	7.66	100	120	50.8	55.5	220	0.505
Chile**	04/01/14	23:46	-19.64	-70.82	27.5	8.12	100	120	108.4	97.5	220	0.579
Ecuador*	04/16/16	23:58	0.382	-79.922	21	7.80	100	120	60.2	---	220	0.537
Solomon*	12/08/16	17:38	-10.68	161.33	41	7.80	100	120	48.4	---	220	0.511
Chile*	12/25/16	14:42	-43.41	-73.94	38	7.60	80	120	42	---	190	0.353
Uncertain												
Vanuatu	10/07/09	22:03	-13.01	166.51	35.4	7.64	80	120	48.8	60	220	0.904
*** GCMT duration** ****130 s duration for early aftershock**												

or Pdiff body wave arrival and later PP and PKiKP arrivals is long enough (> 4 minutes) to be able to measure coda amplitudes robustly as in Fig. 2.5. For short duration sources, observations at closer distances could be considered and a similar procedure to what we develop here can be applied, but our initial focus is on very large tsunamigenic earthquakes that have direct P arrival durations of ~42 to ~178 s.

First-arriving P or Pdiff onsets ($T_{Parrival}$) were picked manually for each event. Event-dependent time windows for the duration of direct phases from the rupture ($\Delta T_{Pdur}=T_{Pend}-T_{Parrival}$) and for the coda portion ($\Delta T_{codadur} = T_{codaend}-T_{Pend}$) of the signals were defined in each case. To specify ΔT_{Pdur}, we mainly use source time function durations from finite-fault inversions by Ye et al. (2016), adding 20 s to account for the arrival of depth phases. If the rupture duration estimate from Global Centroid-Moment Tensor (GCMT) inversion, given by twice the centroid time shift, exceeded that from Ye et al. (2016) by 20 s or more, or we did not have a finite-source model, the GCMT rupture duration time plus 20 s was used to define ΔT_{Pdur}. $T_{codaend}$ is determined by the IASP91 model differential arrival time of the PP phase or the PKiKP phase relative to the P wave at the closest epicentral distance of the data used (80°-100°) and the largest distance used (115°-120°), respectively. It is desirable for $\Delta T_{codadur}$ to be at least the length of ΔT_{Pdur}. This motivates using data at epicentral distances beyond 80°, particularly for very large ruptures, to provide sufficiently large PP-P intervals. $T_{codaend}$ ranged from 190 s to 220 s (relative to $T_{Parrival}$), for minimum distances from 80° to 100°, respectively. For events with very

long rupture durations (> 90 s), the data interval was limited to 90°-115° or 100°-115°, and $T_{codaend}$ was set to a maximum of 255 s to provide enough coda length for a stable measure. The minimum (min GARC) and maximum (max GARC) epicentral distances for the data, Tcodaend, extended GCMT duration (GCMT Td), and extended finite-fault duration (Ye et al. Td) for each event are indicated in Tables 1.1 and 1.2. For rapid implementation, using twice the centroid time from a rapid W-phase inversion with 20 s padding would give a reasonable estimate of ΔT_{Pdur}. $\Delta T_{codadur}$ could be defined rapidly using the distance range of the data and theoretical PP and PKiKP arrival times.

2.2 Shallow Slip Event Specification

The events selected for analysis were bimodally characterized as either having evidence for shallow rupture or not, based on inspection of the finite-fault inversions from Ye et al. (2016) (Supplement S1) along with additional studies in the literature for more recent events. Some events have been well-characterized as shallow-rupturing tsunami earthquakes, including 1992 Nicaragua, 1994 Java, 2/21/1996 Peru, 2006 Java, 2010 Mentawai (e.g., see summaries and references in Lay and Bilek, 2007; Sladen and Trevisan, 2018). Some very large events have been shown to have significant slip extending to the trench in studies additional to Ye et al. (2016), including 2010 Maule (e.g., Yue et al., 2016), 2011 Tohoku (e.g., Lay, 2018; Yamazaki et al., 2018), 2015 Illapel, Chile (e.g., Li et al., 2016; Melgar et al., 2016). Some events appear to have no slip at shallow depth, including 2003 Tokachi, Japan,

2005 Nias, 2007 Pisco, Peru, 2007 Chile, 2007 Sumatra, 2012 Costa Rica, 2016 Chile (Lay, 2015; Sladen and Trevisan, 2018). Based on the many published works and judging those that have the best data constraints for resolving shallow slip if it occurred (mainly based on tsunami modeling, offshore geodetic data, repeat surveying of the bathymetry, etc.), events were bimodally labeled as those with evidence for at least some shallow slip in Table 1.1 and those that appear to lack any shallow slip in Table 1.2. The bimodal classification is uncertain for 2 events included as possibly having shallow slip in Table 1.1 (2009 Papua, 2012 Haida Gwaii) due to these ruptures being on secondary thrust faults without a deep trench (both can be viewed as intraplate ruptures). The 2009 Vanuatu event in Table 1.2 is uncertain as the event is preceded ~20 minutes earlier by a deep M_W 68 rupture for which secondary arrivals may contaminate the coda.

2.3 Data and Root Mean Square Pcoda/P Ratios

For each event, the broadband signals were recursively deconvolved by their instrument responses and filtered in the broad passband 5 to 200 s using a 4^{th}-order two-pass (acausal) Butterworth filter. Example azimuthal profiles of the resulting deconvolved ground displacements and ground velocities for several events are shown in Figures 2.7 to 2.9. Corresponding profiles for all 39 events are shown in Supplementary S2. The profile in Figure 2.7 is for the 2015 Illapel earthquake mentioned above, which is believed to have ruptured with substantial slip to near the trench. The signals have persistent ringing in the coda window with a dominant

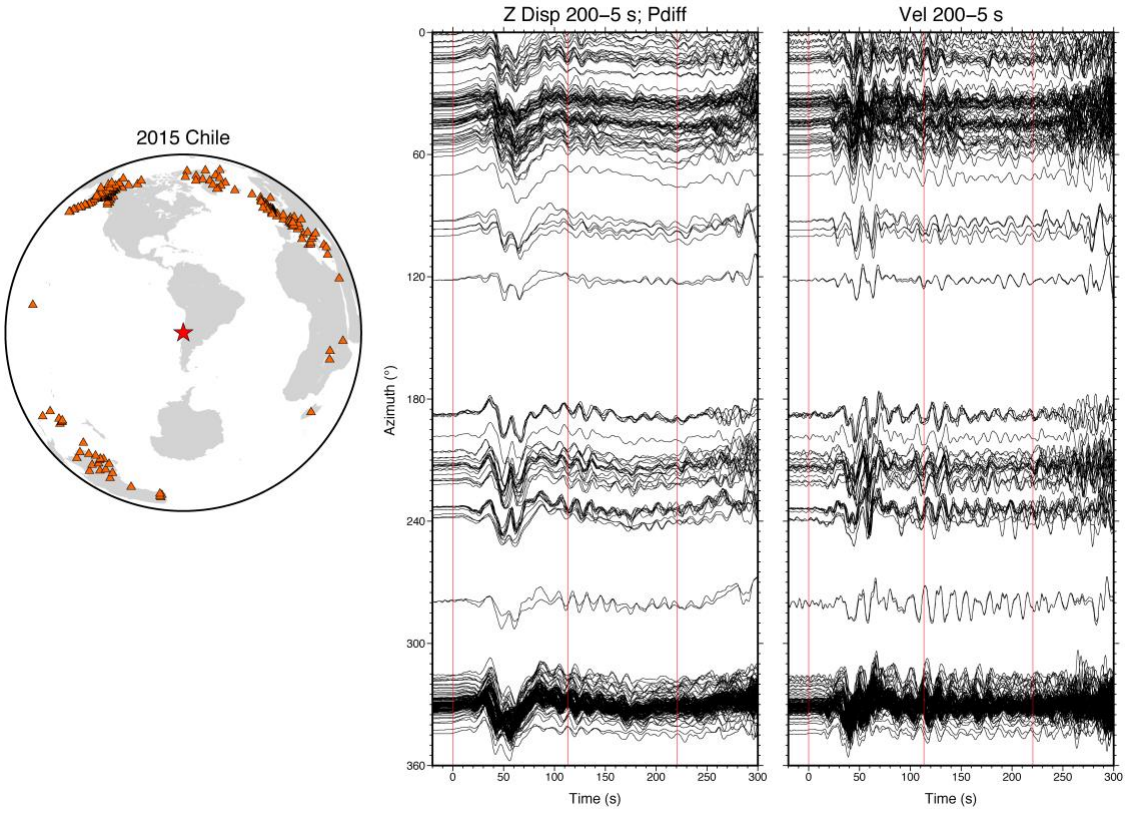

Figure 2.7. Teleseismic recordings for the September 16, 2015 Illapel, Chile earthquake (M_W 8.3). Station distribution and azimuthal profiles of broadband vertical component deconvolved ground displacements (Z Disp) and ground velocities (Vel) band-pass filtered with a causal fourth-order Butterworth bandpass filter with corners at 200 s and 5 s. The stations are in the distance range 100 to 120°. The red star indicates the location of the source with the triangles showing the station locations. The red lines on the profiles indicate the time intervals for the P wave signal from the source (first interval is ΔT_{Pdur}) and the P coda (second interval is $\Delta T_{codadur}$). Note the high levels of oscillatory motion in the coda for this event, which is thought to have rupture extending to the trench.

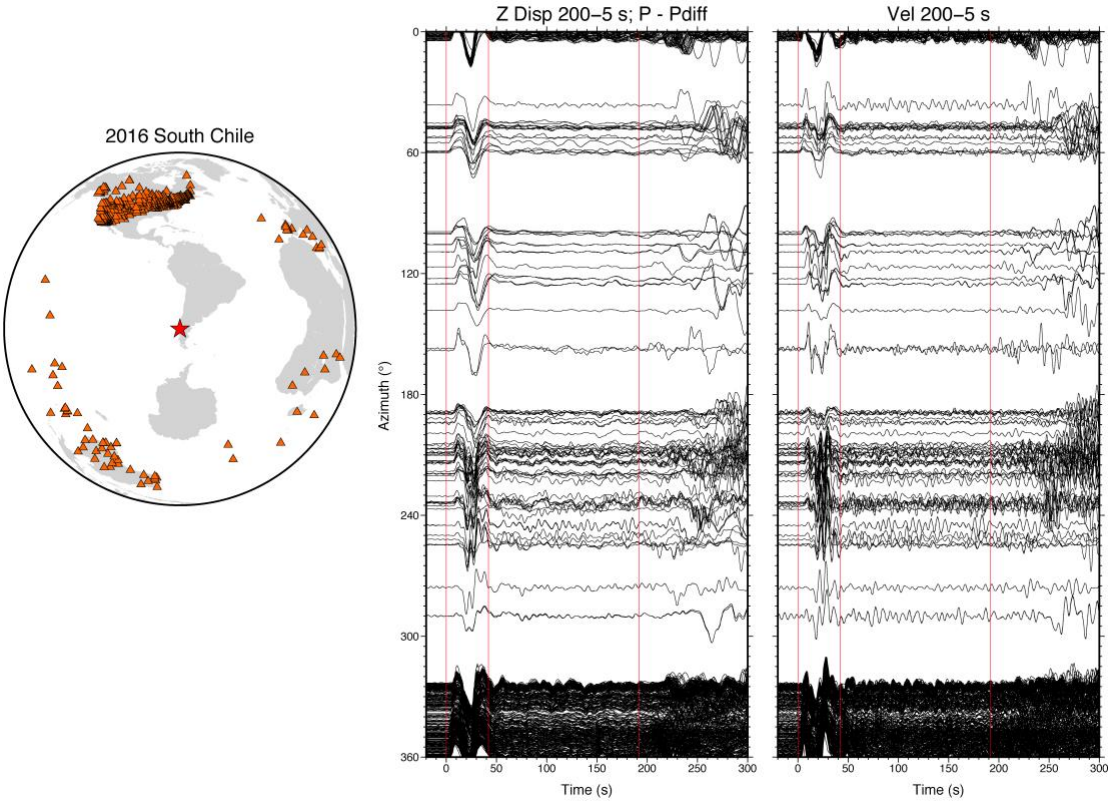

Figure 2.8. Teleseismic recordings for the December 25, 2016 Chile earthquake (M_W 7.6). Station distribution and azimuthal profiles of broadband vertical component deconvolved ground displacements (Z Disp) and ground velocities (Vel) band-pass filtered with a causal fourth-order Butterworth bandpass filter with corners at 200 s and 5 s. The stations are in the distance range 80 to 120°. The red star indicates the location of the source with the triangles showing the station locations. The red lines on the profiles indicate the time intervals for the P wave signal from the source (first interval is ΔT_{Pdur}) and the P coda (second interval is $\Delta T_{codadur}$). Note the fairly low levels of oscillatory motion in the coda for this event, which is not believed to have had rupture extend to the trench.

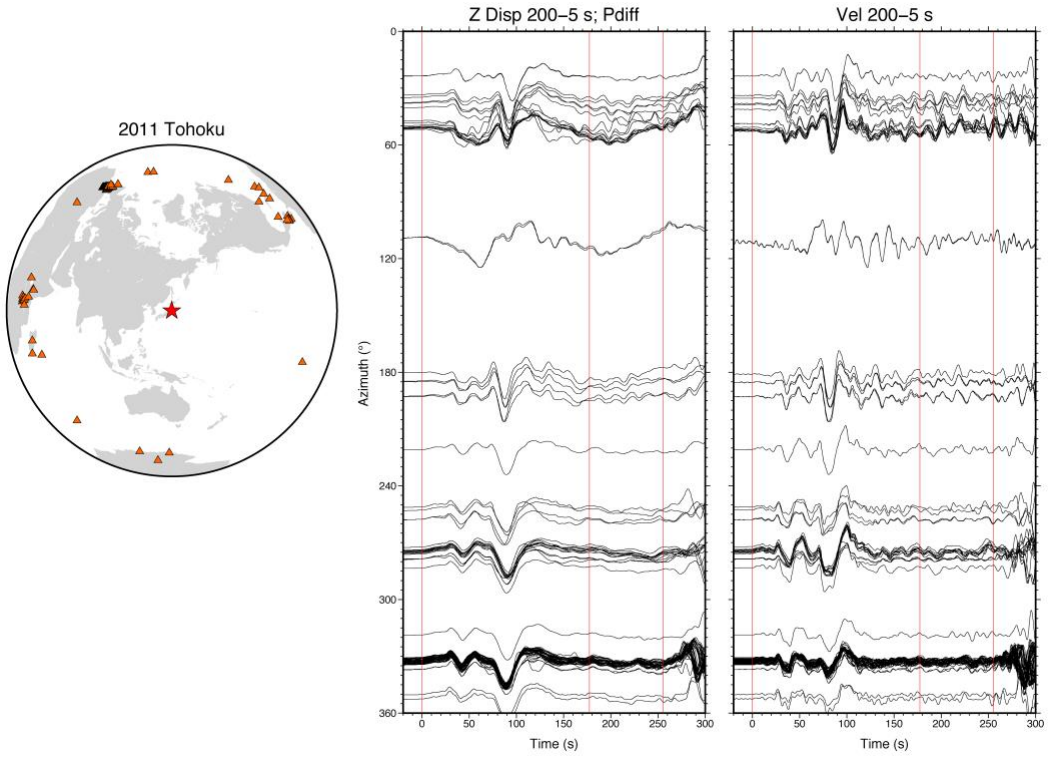

Figure 2.9. Teleseismic recordings for the March 11, 2011 Tohoku, Japan earthquake (M_W 9.1). Station distribution and azimuthal profiles of broadband vertical component deconvolved ground displacements (Z Disp) and ground velocities (Vel) band-pass filtered with a causal fourth-order Butterworth bandpass filter with corners at 200 s and 5 s. The stations are in the distance range 100 to 115°. The red star indicates the location of the source with the triangles showing the station locations. The red lines on the profiles indicate the time intervals for the P wave signal from the source (first interval is ΔT_{Pdur}) and the P coda (second interval is $\Delta T_{codadur}$). Note the broadband coda has variable level relative to the large long-period P energy.

period of about 10 s. This slowly decaying ringing is intrinsically emphasized in the ground velocities. The profile in Figure 2.8 is for the 2016 Southern Chile earthquake, which does not appear to have shallow slip. The coda interval has generally low amplitudes and the traces that do have any ringing have oscillations with less than 8 s period. Note the large concentration of observations at the northern azimuth from the Transportable Array. The non-uniform distribution of observations motivates azimuthal binning of the data. The profile in Figure 2.9 is for the 2011 Tohoku, Japan earthquake. This huge event has P waves with very large long-period energy levels, so that any short-period pwP energy in the coda is expected to be relatively low in these broadband records. This motivates narrow-band filtering of the data as in Figure 1.2 to allow for comparable measures between events.

The benefit of narrow band filtering of the data is shown in Figure 2.10 for displacement seismograms for the two largest events in our database; March 11, 2011 Tohoku, Japan and February 27, 2010 Maule, Chile. The azimuthally distributed waveforms are shown filtered in the 250 to 5 s and 20 to 5 s passbands for each event. Note that the persistent coda ringing at some azimuths is clarified in the narrowband filtered data due to suppression of the very large longer period energy that dominates the broadband P wave window (bracketed by the first pair of red lines).

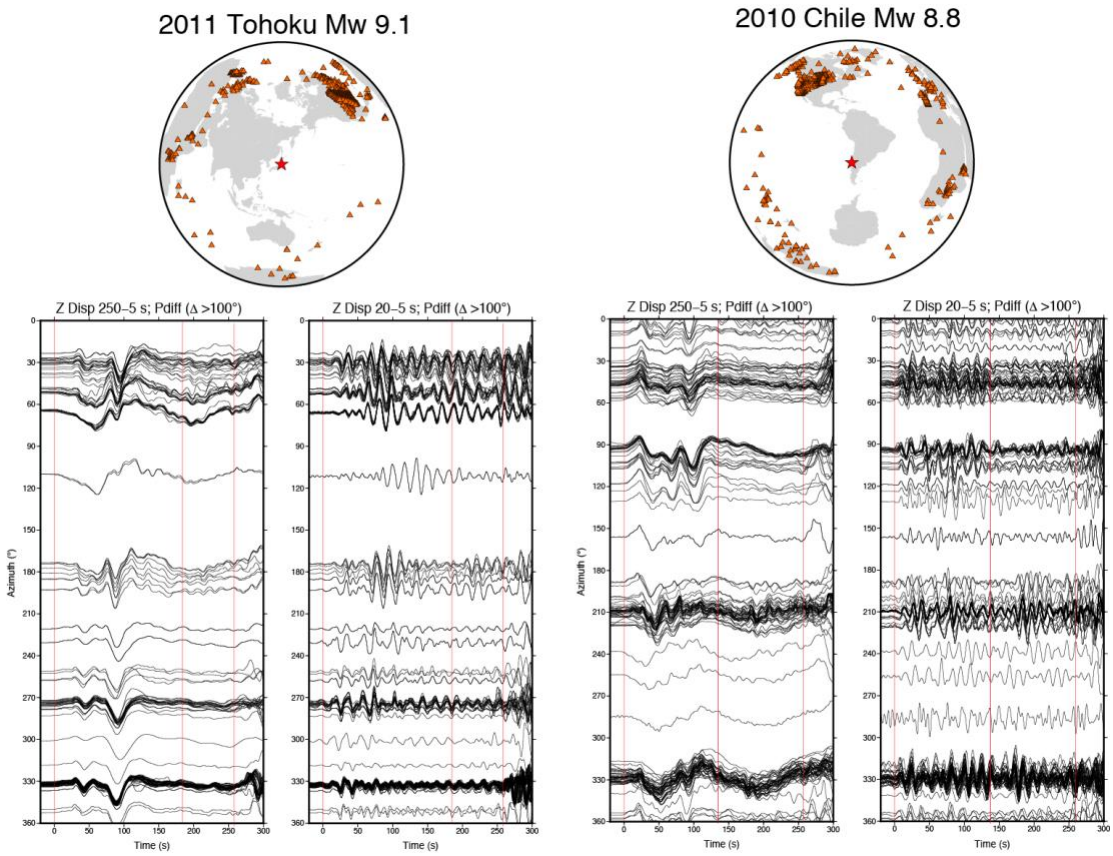

Figure 2.10. Azimuthal plots showing the map view of station distribution and the displacement waveforms with bandpass filters of 250 to 5 s or 20 to 5 s for the two largest earthquakes in the data set; the March 11, 2011 Tohoku earthquake (M_W 9.1) and the February 27, 2010 Maule, Chile earthquake (M_W 8.8).

The general idea of this study is that the signal power in the P coda window will be relatively enhanced if the rupture is efficient in generating pwP that gives persistent oscillations lasting well beyond the source radiation. A measure of the distributed power is thus desired, rather than a magnitude-like peak amplitude, which could be caused by other forms of scattering. Given that the distances that provide long coda windows free of other arrivals include diffracted distances, we do not want to make an absolute measure of the coda with spreading corrections, as the absolute levels will

largely just reflect the event size. Our objective is a simple measure that captures the power in the coda relative to the power in the direct P signal in order to detect relative enhancement of coda resulting from shallow slip, so we use a power ratio approach.

The root mean square (rms) of the broadband ground velocity and the rms spectral amplitude of the ground velocity in the narrowband filtered period range of 7-15 s were calculated for both ΔT_{Pdur} and $\Delta T_{codadur}$ windows for each record in the selected distance range. The narrowband filter period range was designed to emphasize energy in the typical passband of deep-water multiples and to suppress the longer period signal that dominates the direct P window for the very large events as in Figures 1.2 and 2.9. Other narrowband windows were considered, but the 7-15 s window is preferred, as it emphasizes deep water reverberations. Profiles for all events filtered in this passband are shown in Supplement S3. The ratio of rms Pcoda/rms P for the broadband and narrowband signals was then calculated for each seismogram. Event averages of the rms ratios are calculated for each event. As apparent in Figures 2.7 to 2.9 the azimuthal distribution of signals is not uniform among events due to event location and station distribution, and this is especially true for sparser data sets for events before 2000 (see profiles in S2 and S3). Averaging of the ratios in azimuthal bins of from 10° to 30° was performed to improve the uniformity of the data distributions; we ultimately prefer the 10° azimuthal windowing as it best balances the data distribution for both earlier sparse data sets and for more recent dense data sets.

3. Results

3.1 rms Pcoda/P

Azimuthal averaging bins of 10° are used for computing all of the final event average rms Pcoda/rms P (designated as RMS C/P) ratios (Figure 3.1, Tables 1.1 and 1.2). For the narrowband filtered (7-15 s) data, event average RMS C/P ratios above 0.610 are found exclusively for events that are believed to have ruptured to shallow depths, while ratios < 0.610 are found for all but one of ruptures that did not extend to the trench. The two events with shallow slip but no deep trench (2009 Papua and 2012 Haida Gwaii) have low RMS C/P ratios, consistent with the absence of deep water pwP. The 2009 Vanuatu event, which appears to be a deeper rupture does have a high RMS C/P ration, but this may at least partially be due to contamination from the preceding 6.8 deep earthquake. The one clear exception to the overall pattern is for the November 12, 1996 Peru rupture, which does not have shallow slip in the model of Ye et al. (2016) or in the NEIC finite-fault model. The average RMS C/P values are consistent with the readily observable coda levels in the broadband event profiles (Figures 2.7-2.9, S2), given the very simple processing that has been applied. The measurements provide a promising degree of separation.

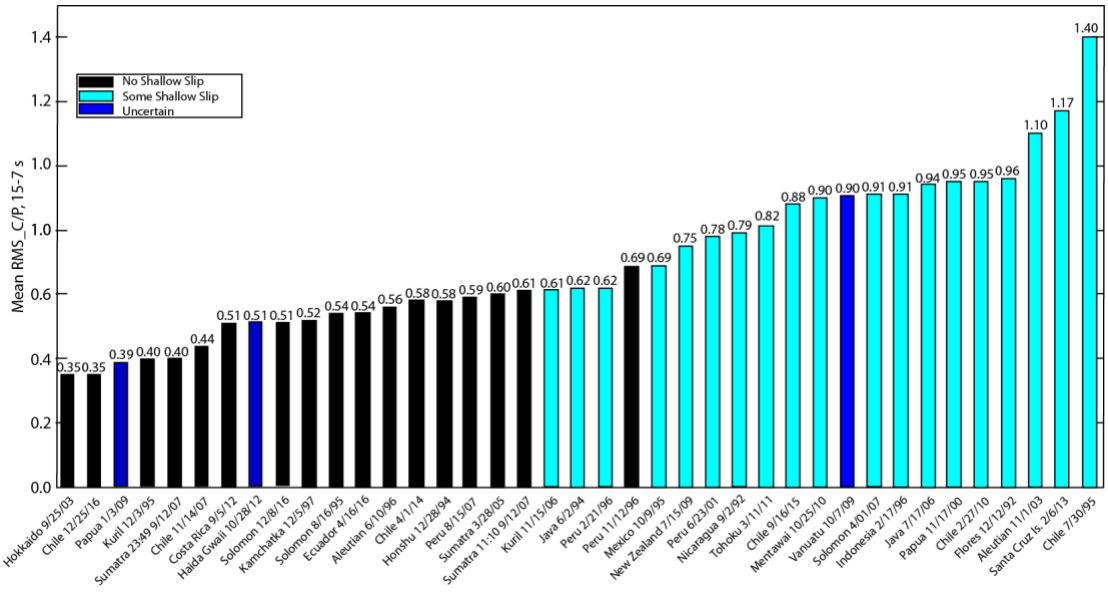

Figure 3.1. Event average RMS C/P ratios ordered by increasing value for all 39 large earthquakes considered in this analysis. Black bars indicate events that are thought to have no shallow slip based on the available slip models, while cyan bars are thought to have at least some shallow slip or only shallow slip. Blue bars indicate events that are ambiguous in their designation.

Recognizing that one expects a continuum of cases with variable amount of shallow slip, it is useful to consider some of the cases with RMS C/P values near the "decision line" of 0.610. The 1994 Java earthquake is identified as a tsunami earthquake, but it has a very concentrated slip pattern (e.g., Abercrombie et al., 2001) and the shallow slip is not as distinctive as for other tsunami events. The 2014 Chile (Iquique) event was found to have a strong early aftershock about 100 s after the mainshock, so the P window was extended to 130 s, resulting in the RMS C/P value of 0.579. The October 9, 1995 Mexico earthquake appears to have some shallow slip in the model of Ye et al. (2016), but it is not well-resolved. The RMS C/P ratio of 0.691 supports enhanced coda excitation by shallow slip. The February 21, 1996 Peru earthquake is classified

as a tsunami earthquake, but has a relatively low RMS C/P of 0.618. The data distribution is spares and largely concentrated in the landward direction from the source, where lower coda is expected, reducing the average value. The June 23, 2001 Peru earthquake is very large and has compound subevent faulting so there is some uncertainty in it slip, but the finite-fault solutions of Pritchard et al. (2007), Lay et al. (2010) and Ye et al. (2016) all suggest that rupture extended to shallow depth. There is also a lack of seaward observations for the 2006 Kuril event, which has a relatively low RMS C/P of 0.610. The individual event data distributions thus warrant detailed consideration.

3.2 Azimuthal patterns in RMS C/P

Several examples of azimuthal distributions of measured RMS C/P for the 7-15 s passband are shown in Figure 3.2 (patterns for all 39 events are shown in Supplement S4). The RMS C/P values tend to be larger at azimuths in the direction of the trench for all cases, and events with deep slip beneath continental margins have pronounced reduction of reverberative coda amplitudes in the landward directions. The azimuthal sampling varies from event to event, so there is potential for bias, but by using large data sets and the 10° azimuthal binning, the average values produce the clear pattern seen in Figure 3.1.

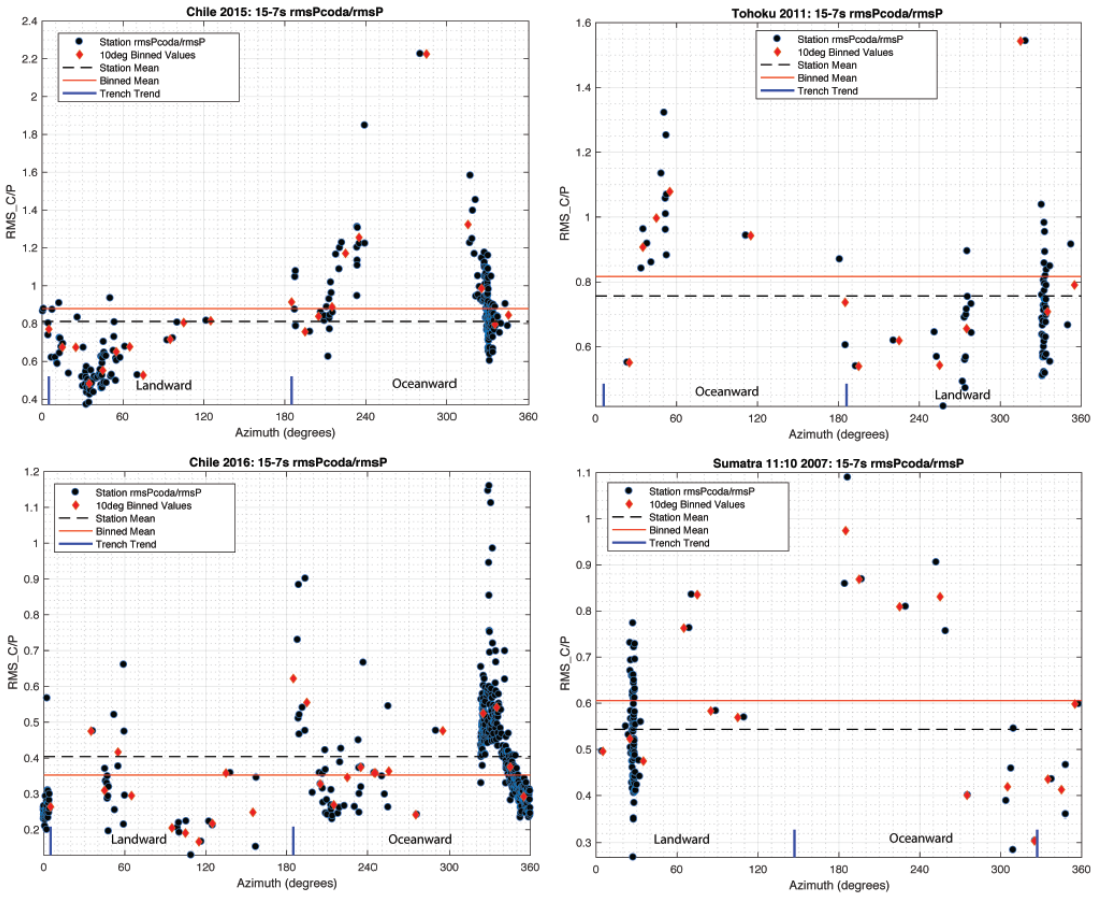

Figure 3.2. Azimuthal plots of RMS C/P measures for four events. The 2015 Chile and 2011 Tohoku events are events believed to have slip to near the trench. The 2016 Chile and 2007 Sumatra event are believed to have slip confinded to deeper on the megathrust. The circles indicate individual station measurements. The diamonds are the mean values in 10° azimuth bins. The dashed line is the mean value of the individual station values. The red line is the mean value of the binned data, which is the value listed in Tables 1.1 and 1.2. The blue ticks indicate the azimuthal trend of the local trench.

4. Discussion

Given that the overall distribution of average RMS C/P is strongly bimodal with respect to the independent constraints on presence or absence of shallow slip (Figure 3.1), similarly measured average RMS ratios above 0.61 should provide a clear

indication of shallow rupture extent and potentially enhanced tsunami excitation. RMS ratios below 0.61 should provide strong indication of no shallow rupture, so tsunami excitation is expected to be primarily controlled by M_W. Intermediate values are ambiguous.

Most events have enhanced coda in the seaward azimuthal direction, whether they have shallow slip or not. This is to be expected from Figure 1.1b, as pwP reverberations in the up-dip direction will encounter deeper and deeper water, even if the slip is deep on the megathrust. However, the overall generation of pwP coda will be enhanced at all azimuths for shallow megathrust slip. We have computed average RMS C/P for binned data at all azimuths, but it is viable to compute average values for limited azimuth ranges, such as just in the seaward direction between the directions of the trench strike. Given the overall success of the classification using all azimuths, which is the simplest for fast implementation, we do not seek an optimal azimuthal windowing measure.

The procedure explored here is remarkably successful in separating ruptures that have shallow slip from those that do not for events larger than M_W 7.5. It is likely to be very effective for smaller events as well, as their entire rupture area will span a smaller depth range than for many of these events. This procedure is of great value for research on large earthquake ruptures and evaluation of their slip extent. It can be applied to historic events that have only limited seismic data for studying the source

process. It may have potential for enhancing confidence of tsunami warnings. Given the 15-18 minute lag time required for measuring numerous relative coda levels in the 80°-120° distance range, our specific procedure is of somewhat limited value for assessing likelihood of enhanced tsunami excitation relative to the seismic moment magnitude of the event for very nearby coastlines. However, it would still have been valuable, for example, for the 2011 Tohoku earthquake where the shallow-slip-generated tsunami did not arrive at the coast until about 30 minutes or more after the event. It should also be possible to define closer distance measures of the relative coda enhancement to give a more prompt assessment of the likelihood of slip having reached to the trench with attendant strong tsunami enhancement. Suppression of the short-period signal contribution from phases like PcP, PP, PPP, S and surface waves will require some windowing rubrics. That will be left for future research efforts.

List of Supplemental Files

S1. Slip Models

S2. Broadband Profiles

S3. Narrowband Profiles

S4. Azimuthal Plots

References

Abercrombie, R. E., M. Antolik, K. Felzer, and G. Ekström (2001). The 1994 Java tsunami earthquake: Slip over a subducting seamount, *Journal of Geophysical Research, 106*, 6595-6607.

Aki, K., and B. Chouet (1975). Origin of coda waves: Source, attenuation, and scattering effects, *Journal of Geophysical Research, 80*, 3322-3342.

An, C., H. Yue, J. Sun, L. Meng, and J. C. Báez (2017). The 2015 M_W 8.3 Illapel, Chile, earthquake: Direction-reversed along-dip rupture with localized water reverberation, *Bulletin of the Seismological Society of America, 107*, 2416-2426, doi:10.1785/0120160393.

Fan, W., and P. M. Shearer (2018). Coherent seismic arrivals in the P wave coda of the 2012 M_W 7.2 Sumatra earthquake: Water reverberations or an early aftershock? *Journal of Geophysical Research: Solid Earth, 123*, 3147-3159, https://doi.org/10.1002/2018JB015573.

Fujiwara, T., S. Kodaira, T. No, Y. Kaiho, N. Takahashi, and Y. Kaneda (2011). The 2011 Tohoku-oki earthquake: displacement reaching the trench axis, *Science, 334*, 1240, http://dx.doi.org/10.1126/science.1211554.

Ihmlé, P. F., and R. Madariaga (1996). Monochromatic body waves excited by great subduction zone earthquakes, *Geophysical Research Letters, 23*, 2999-3002.

Kanamori, H. (1972). Mechanism of tsunami earthquakes, *Physics of Earth and Planetary Interiors, 4*, 289-300.

Kanamori, H. (2014). The diversity of large earthquakes and its implications for hazard mitigation, *Annual Reviews of Earth and Planetary Sciences, 42*, 7-26, doi:10.1146/annurev-earth-060313-055034.

Kanamori, H., L. Rivera, L. Ye, T. Lay, S. Murotani, and K. Tsumura (2019). New constraints on the 1922 Atacama, Chile, earthquake from historical seismograms, *Geophysical Journal International*, in review.

Lay, T. (2015). The surge of great earthquakes from 2004 to 2014, *Earth and Planetary Science Letters, 409*, 133-146.

Lay, T. (2018). A review of the rupture characteristics of the 2011 Tohoku-oki M_W 9.1 earthquake, *Tectonophysics, 733*, 4-36, http://dx.doi.org/10.1016/j.tecto.2017.09.022.

Lay, T., and S. L. Bilek (2007). Anomalous earthquake ruptures at shallow depths on subduction zone megathrusts, in: *The Seismogenic Zone of Subduction Thrust Faults*, Edited by T. H. Dixon and J. C. Moore, Columbia University Press, New York, pp. 476-511.

Lay, T., L. Li, and K. F. Cheung (2016). Modeling tsunami observations to evaluate a proposed late tsunami earthquake stage for the 16 September 2015 Illapel, Chile, M_W 8.3 earthquake, *Geophysical Research Letters, 43*, 7902-7912, doi:10.1002/2016GL070002.

Lay, T., C. J. Ammon, A. R. Hutko, and H. Kanamori (2010), Effects of kinematic constraints on teleseismic finite-source rupture inversions: Great Peruvian earthquakes of 23 June 2001 and 15 August 2007, *Bulletin of the Seismological Society of America, 100*, 969-994, doi:10.1785/0120090247.

Lay, T., H. Kanamori, C. J. Ammon, K. D. Koper, A. R. Hutko, L. Ye, H. Yue, and T. M. Rushing (2012). Depth-varying rupture properties of subduction zone megathrust faults, *Journal of Geophysical Research, 117*, B04311.

Li, L., T. Lay, K. F. Cheung, and L. Ye (2016). Joint modeling of teleseismic and tsunami wave observations to constrain the 16 September 2015 Illapel, Chile, M_W 8.3 earthquake rupture process, *Geophysical Research Letters*, **43**, 4303-4312, doi:10.1002/2016GL068674.

Lee, S.-J., T.-Y. Yeh, T.-C. Lin, Y.-Y. Lin, T.-R. Alex Song, and B.-S. Huang (2016). Two-stage composite megathrust rupture of the 2015 M_W 8.4 Illapel, Chile earthquake identified by spectral-element inversion of teleseismic waves, *Geophysical Research Letters, 43*, 4979-4985, doi:10.1002/2016GL068843.

Maksymowicz, A., C. D. Chadwell, J. Ruiz, A. M.Tréhu, E. Contreras-Reyes, W. Weinreber, J. Díaz-Naveas, J. C. Gibson, P. Lonsdale and M. D. Tryon (2017). Coseismic seafloor deformation in the trench region during the Mw8.8 Maule megathrust earthquake, *Scientific Reports, 7*, 45918, doi:10.1038/srep45918.

Melgar, D., W. Fan, S. Riquelme, J. Geng, C. Liang, M. Fuentes, G. Vargas, R. M. Allen, P. M. Shearer, and E. J. Fielding (2016). Slip segmentation and slow rupture to the trench during the 2015, M_W8.3 Illapel, Chile earthquake, *Geophysical Research Letters, 43*, 961-966, doi:10.1002/2015GL067369.

Melgar, D., S. Riquelme, X. Xu, J. C. Baez, J. Geng, and M. Moreno (2017). The first since 1960: A large event in the Valdivia segment of the Chilean subduction zone, the 2016 M7.6 Melinka earthquake, *Earth and Planetary Science Letters, 474*, 68-75, http://dx.doi.org/10.1016/j.epsl.2017.06.026.

Pritchard, M. E., E. O. Norabuena, C. Ji., R. Boroschek, D. Comte, M. Simons, T. H. Dixon, and P. A. Rosen (2007), Geodetic, teleseismic, and strong motion constraints on slip from recent southern Peru subduction zone earthquakes, *Journal of Geophysical Research, 112*, B03307, doi:10.1029/2006JB004294.

Qian, Y., S. Wei, W. Wu, H. Zeng, A. Coudurier-Curveur, and S. Ni (2019). Teleseismic waveform complexities caused by near trench structures and their impacts on earthquake source study: Application to the 2015 Illapel aftershocks (Central Chile), *Journal of Geophysical Research: Solid Earth, 124*, 870-889.

Sladen, A., and J. Trevisan (2018). Shallow megathrust earthquake ruptures betrayed by their outer-trench aftershocks signature, *Earth and Planetary Science Letters, 483*, 105-113, https://doi.org/10.1016/j.epsl.2017.12.006.

Sun, T., K. Wang, T. Fujiwara, S. Kodaira, and J. He (2017). Large fault slip peaking at trench in the 2011 Tohoku-oki earthquake, Nature Communications, 81, 4044, http://dx.doi.org/10.1038/ncomms14044.

Ward, S. N. (1979). Ringing P waves and submarine faulting, *Journal of Geophysical Research, 84*, 3057-3062.

Wiens, D. A. (1987). Effects of near source bathymetry on teleseismic P waveforms, *Geophysical Research Letters, 14*, 761-764, https://doi.org/10.1029/GL014i007p00761.

Wiens, D. A. (1989). Bathymetric effects on body waveforms from shallow subduction zone arthquakes and application to seismic processes in the Kurile trench, *Journal of Geophysical Research, 94*, 2955-2972, https://doi.org/10.1029/JG094iB03p02955.

Wu, W., S. Ni, Z. Zhan, and S. Wei (2018). A SEM-DSM three-dimensional hybrid method for modeling teleseismic waves with complicated source-side structures, *Geophysical Journal International, 215*, 133-154, https://doi.org/10.1093/gji/ggy273.

Yamazaki, Y., K. F. Cheung, and T. Lay (2018). A self-consistent fault slip model for the 2011 Tohoku earthquake and tsunami, *Journal of Geophysical Research: Solid Earth*, **123**, 1435-1458, https://doi.org/10.1002/2017JB014749.

Ye, L., T. Lay, H. Kanamori, and L. Rivera (2016). Rupture characteristics of major and great ($M_W \geq 7.0$) megathrust earthquakes from 1990 to 2015: 1. Source parameter scaling relationships, *Journal of Geophysical Research: Solid Earth, 121*, 826-844, doi:10.1002/2015JB012426.

Yue, H., T. Lay, L. Rivera, C. An, C. Vigny, X. Tong, and J. C. Báez Soto (2014). Localized fault slip to the trench in the 2010 Maule, Chile M_w 8.8 earthquake from joint inversion of high-rate GPS, teleseismic body waves, InSAR, campaign GPS, and tsunami observations, *Journal of Geophysical Research*, **119**, 7786-7804, doi:10.1002/2014JB011340.

Yue, H., J. C. Castellanos, C. Yu, L. Meng, and Z. Zhan (2017). Localized water reverberation phases and its impact on backprojection images, *Geophysical Research Letters, 44*, 9573-9580, doi:10.1002/2017GL073254.